RSC Advances

PAPER

View Article Online
View Journal | View Issue

Cite this: *RSC Adv.*, 2018, **8**, 33600

Low temperature fabrication of Fe_2O_3 nanorod film coated with ultra-thin g-C_3N_4 for a direct z-scheme exerting photocatalytic activities†

Suhee Kang,[a] Joonyoung Jang,[a] Rajendra C. Pawar,[b] Sung-Hoon Ahn[c] and Caroline Sunyong Lee*[a]

Received 26th May 2018
Accepted 18th September 2018

DOI: 10.1039/c8ra04499f

rsc.li/rsc-advances

We engineered high aspect ratio Fe_2O_3 nanorods (with an aspect ratio of 17 : 1) coated with g-C_3N_4 using a sequential solvothermal method at very low temperature followed by a thermal evaporation method. Here, the high aspect ratio Fe_2O_3 nanorods were directly grown onto the FTO substrate under relatively low pressure conditions. The g-C_3N_4 was coated onto a uniform Fe_2O_3 nanorod film as the heterostructure, exhibiting rational band conduction and a valence band that engaged in surface photoredox reactions by a direct z-scheme mechanism. The heterostructures, particularly 0.75g-C_3N_4@Fe_2O_3 nanorods, exhibited outstanding photocatalytic activities compared to those of bare Fe_2O_3 nanorods. In terms of 4-nitrophenol degradation, 0.75g-C_3N_4@Fe_2O_3 nanorods degraded all of the organic pollutant within 6 h under visible irradiation at a kinetic constant of 12.71×10^{-3} min^{-1}, about 15-fold more rapidly than bare Fe_2O_3. Further, the hydrogen evolution rate was 37.06 μmol h^{-1} g^{-1}, 39-fold higher than that of bare Fe_2O_3. We suggest that electron and hole pairs are efficiently separated in g-C_3N_4@Fe_2O_3 nanorods, thus accelerating surface photoreaction *via* a direct z-scheme under visible illumination.

1. Introduction

Efforts to replace traditional fossil fuels are increasing because of the energy crisis and environmental contamination.[1,2] One of the many fascinating green technologies is photocatalytic degradation of organic pollutants and sustainable hydrogen production employing solar energy.[3–5] Many inorganic,[6] organic,[7] metal,[8] metal oxide,[9–13] and non-metal[14] materials have been used to reduce wastewater pollution and generate sustainable energy. However, the rapid recombination rates of charge carriers on catalytic surfaces reduce the photocatalytic efficiencies of single-component catalysts. Thus, semiconductor-based photocatalysts have received considerable attention; heterostructures of many materials afford reasonable band levels, maximizing rapid photocatalysis.[15–18] As the conduction and valence band levels differ, electron/hole pairs created using solar energy do not readily combine, improving photocatalytic performance. Nevertheless, heterostructure photo-oxidation/reduction reactions are compromised by the short energy bands of heterostructures compared to single-phase materials.[19]

The direct z-scheme, which recombines weaker oxidative holes and reductive electrons from semiconductors, has emerged as a major research area because the scheme may improve surface charge transfer and separation.[20–22] Various direct z-scheme photocatalysts have been studied, including g-C_3N_4/Ag_3PO_4,[23] Fe_2O_3/Cu_2O,[24] and Bi_2O_3/g-C_3N_4.[25] However, these heterostructures lack stability when exposed to sunlight and are difficult to synthesize. Useful heterostructures would be simply synthesized and exhibit excellent stability.

Recently, graphitic carbon nitride (g-C_3N_4), a polymeric non-metallic semiconductor, has been widely studied as a photocatalyst. Fabrication is inexpensive and simple, the material is carbon/nitrogen-rich and is non-toxic.[26] Furthermore, g-C_3N_4 exhibits a band gap of 2.6 eV, which is eminently suitable in terms of pollutant degradation and hydrogen evolution.[27–29] However, pure g-C_3N_4 exhibits rapid recombination of photogenerated electron/hole pairs, severely compromising photocatalytic activity. To reduce the recombination rate, heterostructures using different conduction and valence bands to host (reducing) electrons and (oxidizing) holes are required.[30–34]

The transition metal oxide Fe_2O_3 can utilize solar light of wavelengths up to 600 nm; the band gap is ~2.1 eV. Thus, Fe_2O_3 exhibits great potential because of its low cost, abundance, and good chemical stability.[35] Moreover, Fe_2O_3 has a 2.38 eV valence

[a]Department of Materials and Chemical Engineering, Hanyang University, Ansan, Gyeonggi-do, 15588, South Korea. E-mail: sunyonglee@hanyang.ac.kr
[b]Department of Energy Engineering, Hanyang University, Seoul, 04763, South Korea
[c]Department of Mechanical and Aerospace Engineering, Seoul National University, Seoul, 08826, South Korea

† Electronic supplementary information (ESI) available. See DOI: 10.1039/c8ra04499f

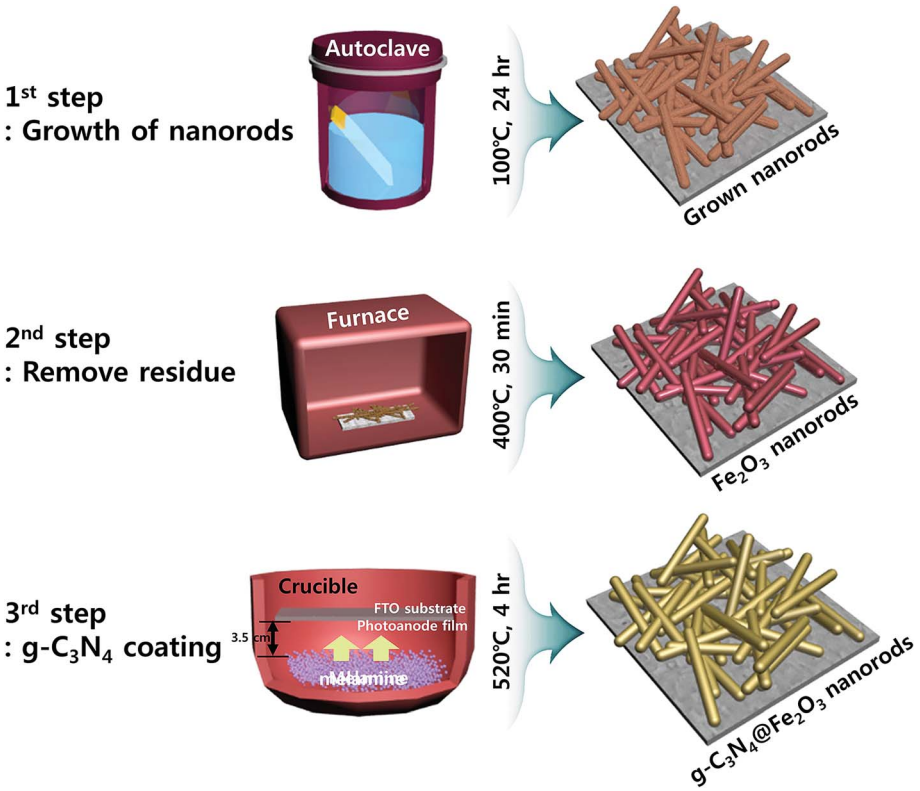

Scheme 1 Fabrication of facile and simple heterostructures of g-C_3N_4@Fe_2O_3.

band that can be exploited by the direct z-scheme mechanism of photocatalysis; thus, Fe_2O_3 can serve as a photoactive material.[36] However, Fe_2O_3 has a short hole diffusion length and exhibits rapid charge recombination, rendering the photocatalytic efficiency low.[37] Therefore, Fe_2O_3 must be combined with other semiconductors in heterostructures featuring separation of electron/hole pairs, allowing photo-oxidation and reduction using the direct z-scheme system.

Many Fe_2O_3/g-C_3N_4 heterostructures, including powder-like bulk composites, have been developed to eliminate organic pollutants and evolve H_2 under visible irradiation.[38–41] However, such heterostructures, when exposed to solar illumination, exhibit gradual reductions in electron movement, compromising photocatalysis compared to that of one-dimensional (1D) structures.[42] To overcome this problem, we fabricated g-C_3N_4@1D Fe_2O_3 nanorods using the simplest procedure; *In situ* growing of high aspect ratio of Fe_2O_3 nanorods with solvothermal method at 100 °C for 24 hours was followed by ultrathin coating of g-C_3N_4 layer using melamine precursors with thermal evaporation method to degrade 4-nitrophenol (4-NP) and evolve H_2. The prepared 1D Fe_2O_3 nanorods coated with ultra-thin g-C_3N_4 layers can be fabricated in a straightforward, cost-effective manner to show the direct z-scheme system. We explored the physicochemical properties of our materials and optimized the g-C_3N_4@Fe_2O_3 nanorods in terms of photocatalysis; we then compared the materials to that of bare Fe_2O_3 nanorods for its potential application in photocatalytic fields such as H_2 evolution, artificial photosynthesis or even more electrocatalysts and battery applications.

2. Experimental

2.1 Materials

We used the Fe_2O_3 precursor ferric chloride ($FeCl_3$) and the g-C_3N_4 precursor melamine (Junsei, Japan). Sodium nitride ($NaNO_3$), hydrochloric acid (HCl), acetonitrile, sodium sulfate (Na_2SO_4) and hydrogen peroxide (H_2O_2) were all purchased from Daejung (Korea). Triethanolamine (TEOA) (Samchun, Korea) and H_2PtCl_2 (Sigma-Aldrich, USA) were used to trigger H_2 evolution. Conductive fluorine-doped tin oxide (FTO, 15 mΩ) served as the photoanode film. *p*-nitrophenol was purchased from Kanto (Japan). All chemicals were used without further purification.

2.2 Preparation of a Fe_2O_3 photoanode and g-C_3N_4 coating

Fe_2O_3 photoanodes were prepared on FTO substrates using a solvothermal method under relatively low pressurized condition.[43] Conventionally, pressurized condition is mostly used for fabrication of Fe_2O_3 photoanodes. However, we have developed relatively low pressure process to fabricate high aspect ratio of nanorods (almost 17 : 1) film with extreme uniformity onto FTO substrate through *in situ* process. Prior to Fe_2O_3 growth, the substrates were sequentially cleaned with acetone, ethanol, and distilled water with sonication for 5 min each time and dried in an oven. 0.2 M $FeCl_3$ was dissolved in 35 mL of distilled water while 1.4 M $NaNO_3$ and 0.5 mL of HCl were added. After complete dissolution, 15 mL of acetonitrile was added and this mixture was stirred for 30 min. Plasma-enhanced chemical vapor deposition (PECVD) was used to perform O_2 plasma

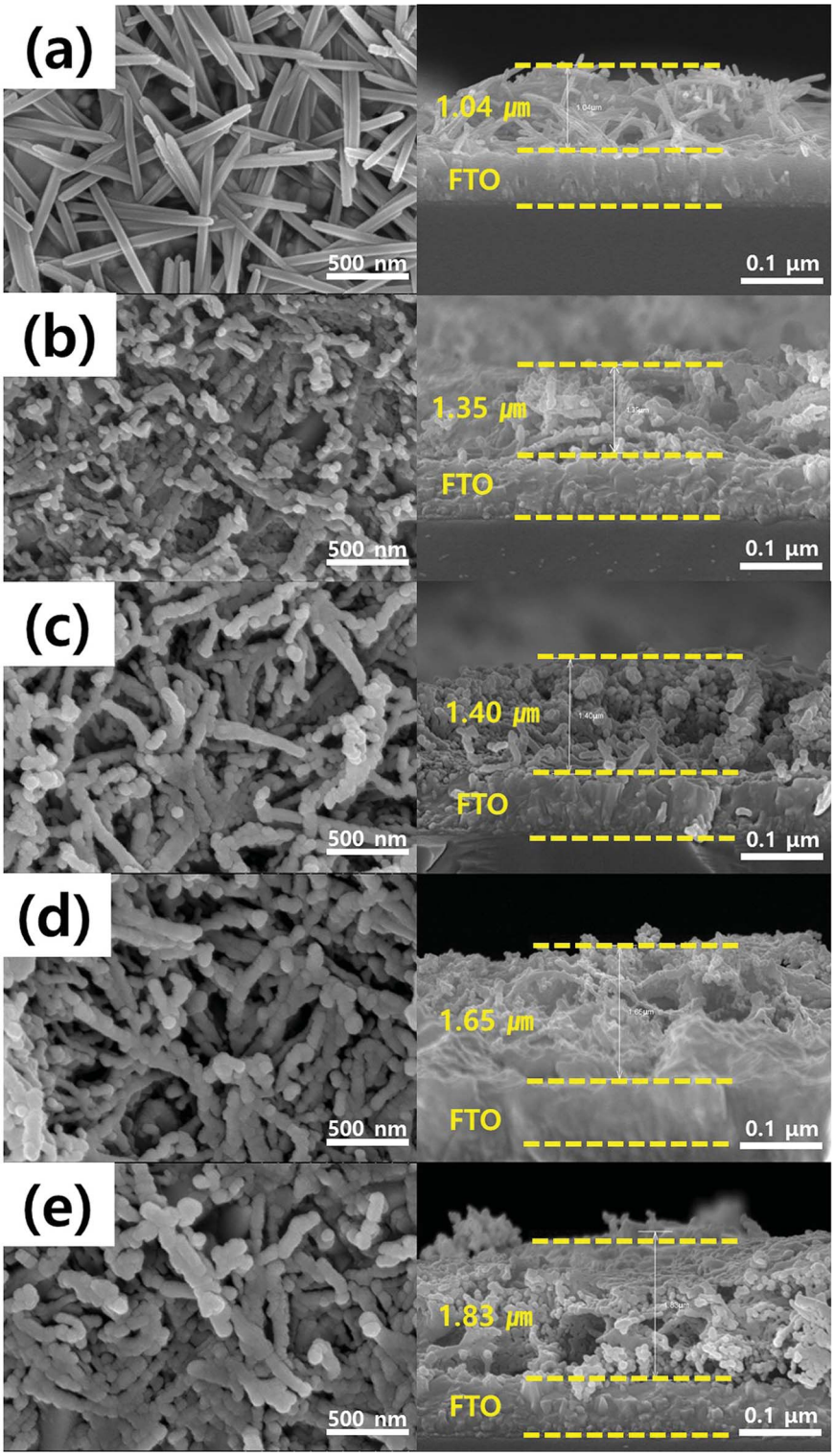

Fig. 1 SEM micrographs of (a) bare Fe_2O_3, (b) 0.25g-C_3N_4@Fe_2O_3, (c) 0.5g-C_3N_4@Fe_2O_3, (d) 0.75g-C_3N_4@Fe_2O_3, and (e) 1g-C_3N_4@Fe_2O_3; cross-sections (right-hand) and surface views (left-hand).

treatment, removing any pollutants. The solution described above was transferred to 100 mL of Teflon-lined molds and held at 100 °C for 24 h in a box furnace. Afterwards, the film was taken out from the mold and dried at ambient atmosphere. Then, the dried film was annealed at 400 °C for 30 min and washed several times with distilled water in order to remove any residues left on the top of the film. Fig. S1(b)† shows no transformation of this material to hematite phase after annealing at 400 °C since no peak for hematite is detected. In order to make successful transformation to hematite Fe_2O_3

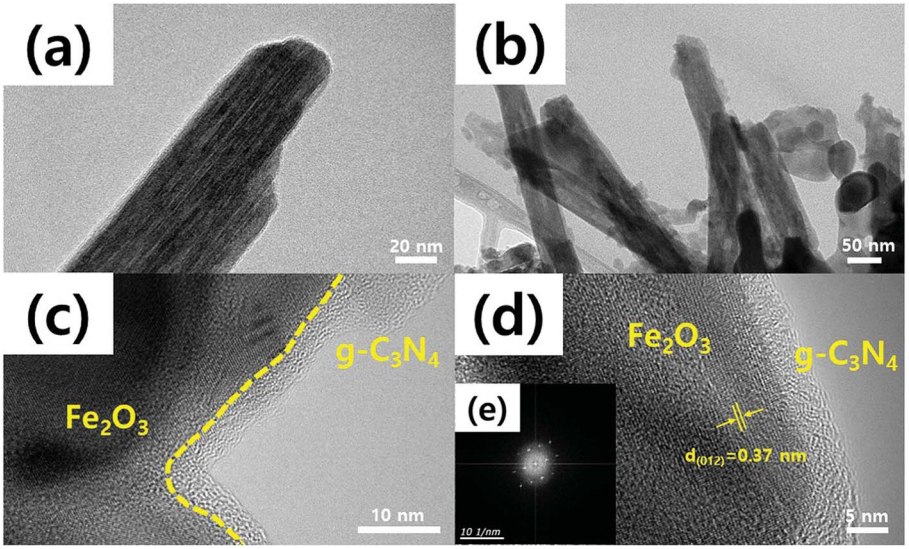

Fig. 2 Transmission electron microscopy (TEM) images of (a) bare Fe_2O_3 nanorods and (b) 0.75g-C_3N_4@Fe_2O_3. (c) High-magnification image of the g-C_3N_4 coating layer on Fe_2O_3 nanorods. (d) The lattice distance of Fe_2O_3 and (e) the fats Fourier transform (FFT) [inset in (d)].

phase, this washed film was annealed again at 520 °C for 4 h where this is denoted as "bare Fe_2O_3" for clarification. To coat the photoanodes with a g-C_3N_4 layer to form heterostructure, various amounts of melamine (0.25, 0.5, 0.75, and 1 g) in powder form were used in alumina crucible for optimization of heterostructure. Photoanode film was placed 3.5 cm apart from the melamine powders, facing each other in the crucible as shown in Scheme 1. Then, the melamine powders were sintered and coated on the surface of the photoanode film through thermal evaporation method at 520 °C for 4 h (10 °C min^{-1}). Finally, g-C_3N_4-coated photoanode films were successfully obtained by this evaporation of melamine powders as the overall procedure is represented in Scheme 1.

2.3 Evaluation of photocatalytic activity

Photocatalytic activity was evaluated using 0.02 mM 4-NP in distilled water. The g-C_3N_4@Fe_2O_3 photoanode films were placed in 250 mL amounts of this solution and 0.5 mL of H_2O_2 was added prior to illumination to accelerate catalytic activity, followed by stirring for 30 min in the dark. The H_2O_2 is used to produce hydroxyl radical (·OH) and OH^- species, reducing Fe^{3+} to Fe^{2+} under light condition.[51] Then, 300W Xe arc lamp (>400 nm cut-off filter) was used to illuminate the solution while amount of 3 mL was collected every 1 h until the degradation was complete.

2.4 Photoelectrochemical performance

Photoelectrochemical (PEC) performance was evaluated using a three-electrode in quartz cell. Graphite and Ag/AgCl served as the counter-electrode and reference electrode, respectively. The electrolyte solution was 0.5 M Na_2SO_4 and PEC performance was analyzed using a Xe arc lamp (300 W, model 66984; Oriel, USA) with cut-off filter (>400 nm). A transient photocurrent was applied at 1 V of bias potential *versus* the Ag/AgCl reference electrode, with light-chopping every minute to allow the response to be observed. Stability testing was performed for 40 h under the same conditions. Linear sweep voltammetry (LSV) was performed at a 20 mV s^{-1} scan rate from −1 to 1 V. Electrochemical impedance spectroscopy (EIS) was performed from 10^5 to 0.01 Hz at an amplitude of 20 mV under both dark and light conditions.

2.5 Photocatalytic H_2 production

Photocatalytic H_2 evolution was assessed with the aid of a 250 mL quartz reactor in a closed-gas system under visible illumination. The light source was a 300 W Xe arc lamp fitted with an ultraviolet (UV) cut-off filter (>400 nm), thus delivering only visible light. 10 mg of as-prepared catalytic powder were dispersed in135 mL of distilled water until they are completely mixed. Then, 9 vol% of TEOA was added into that of aqueous solution to be acted as hole capture. A 1 wt% Pt solution served as the co-catalyst *via in situ* photodeposition. The solutions were uniformly dispersed prior to reaction. The suspension was then transferred to the quartz reactor and purged with N_2 gas to remove O_2. The reactor was sealed with a septum and purged with Ar gas to completely eliminate all air. Evolved gas was detected by a pulsed discharge detector fitted to a gas chromatograph (model 6500GC; YL Instruments, Korea); helium served as the carrier gas.

2.6 Characterization

g-C_3N_4 and Fe_2O_3 morphologies were studied using a scanning electron microscope (SEM; model S4800; Hitachi, Japan) and a transmission electron microscope (TEM) (model JEM 2100F; JEOL, Japan). The crystalline structure and other properties of the Fe_2O_3 phase were analyzed by X-ray diffraction (XRD) (D/Max-2500/PC instrument; Rigaku, USA; Cu-Kα source), Fourier-transform infrared spectroscopy (FTIR) (iS10

instrument; Thermo Fisher Scientific, UK), and X-ray photoelectron spectroscopy (XPS) (Sigma Probe instrument, Thermo Fisher Scientific; Al Kα source); these modality es were also used to confirm the presence of g-C_3N_4 coatings. The band gap energy was calculated *via* UV-visible spectroscopy (UV-Vis) (model V650; JASCO, Japan). Photoluminescence (PL) (SC-100 instrument; Dongwoo, Korea) and Raman spectroscopy (S-Ram instrument; Dongwoo) were employed to monitor the recombination rate of Fe_2O_3 and g-C_3N_4 under light excitation at 325 nm. All PEC analyses were performed using a potentiostat (Versastat 4 instrument; Princeton Applied Research, USA). The absorbances of photocatalytically degraded solutions were measured *via* UV-Vis spectroscopy.

3. Results and discussion

3.1 Morphology

We fabricated heterostructures using sequential solvothermal and thermal evaporation methods. We obtained top and cross-sectional views to explore how morphologies varied by the extent of coating. Prior to structural observations, chemically grown photoanode films were annealed first at 400 °C for 30 min and then washed several times with distilled water to remove any residue within nanorods that might interfere with electron transfer. As a result, the microstructure showed that the residue was perfectly removed while these nanorods are still strongly attached to the FTO substrate even after washing (Fig. S1(a)†). However, the annealing process at 400 °C for 30 min followed by washing treatments did not convert its structural phase into hematite phase since high intensity of $NaNO_3$ peaks (JCPDS no. 36-1474) and SnO_2 peaks (JCPDS no. 77-0451) were shown in Fig. S1(b).† To obtain pure hematite Fe_2O_3 nanorods, washed photoanode film was again annealed at 520 °C for 4 h. And finally, the bare Fe_2O_3 film was acquired.

As shown in Fig. 1(a), the FTO substrate contained only Fe_2O_3 nanorods, the surfaces of which were smooth. The observed high aspect ratio would be expected to improve electron transfer and photoactivity (Fig. S2†). After the g-C_3N_4 precursor was evaporated during optimum sintering at 520 °C, nano-sized, agglomerated g-C_3N_4 particles were clearly attached to the Fe_2O_3 nanorods. The thicknesses of these microstructures averaged around 1.5 μm (from the bottom of the Fe_2O_3 nanorod to the top of the g-C_3N_4 coating). The thickness of the heterostructured films increased as the amount of the melamine precursor increased, from 0.25 to 0.5, 0.75 and 1 g, resulting in increasing thermal evaporation of g-C_3N_4 [Fig. 1(b)–(e)]. A previous study indicated that the precursor level should be varied to optimize the coating layer; thicker layers obstruct incident light and reduce activity.[45] We performed energy-dispersive spectroscopy (EDS) mapping to reveal the elements of g-C_3N_4@Fe_2O_3 heterostructures; these were (as expected) iron, oxygen, carbon, and nitrogen (Fig. S3†). For comparison, the bulk g-C_3N_4 was observed for its microstructures in terms of agglomeration, reducing the active site from surface area as well as blocking electron pathway under illumination as shown in Fig. S4.† We thus confirmed that well-formed g-C_3N_4@Fe_2O_3 heterostructures had been created *via* a simple chemical process.

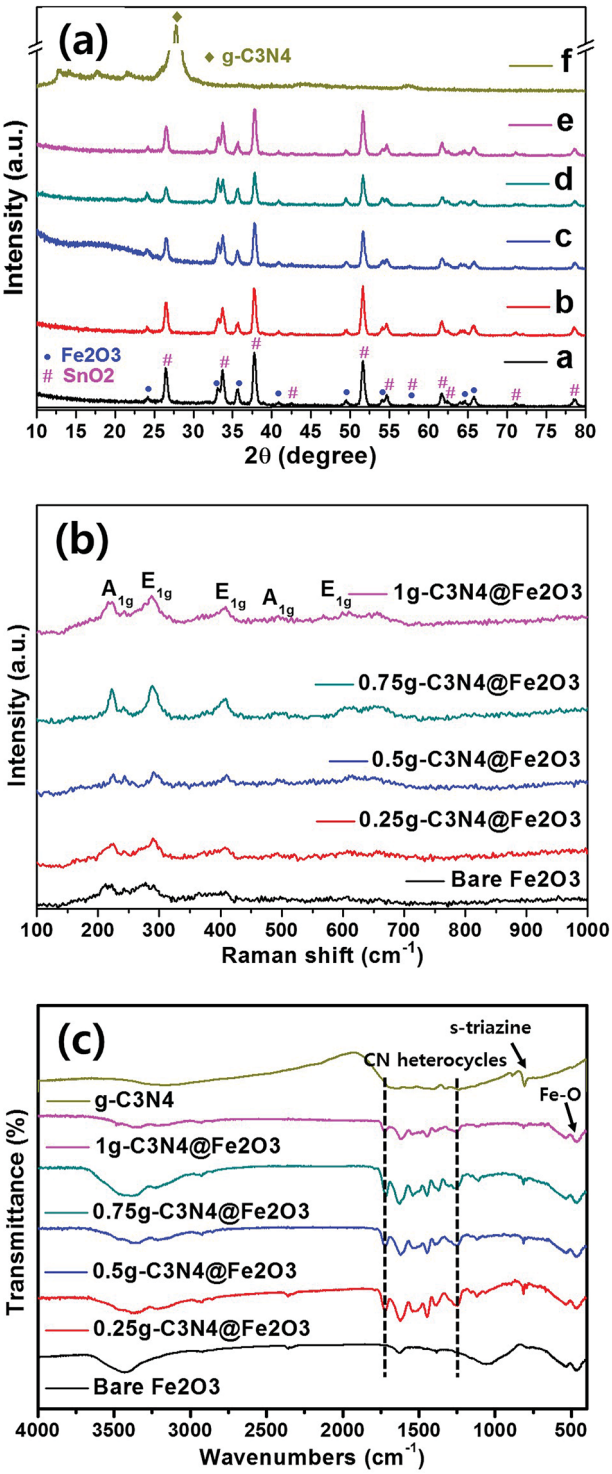

Fig. 3 (a) X-ray diffraction (XRD), (b) Fourier-transform infrared spectroscopy (FT-IR) and (c) Raman spectroscopy data for bare Fe_2O_3, 0.25g-C_3N_4@Fe_2O_3, 0.5g-C_3N_4@Fe_2O_3, 0.75g-C_3N_4@Fe_2O_3, 1g-C_3N_4@Fe_2O_3 and bulk g-C_3N_4.

The TEM was used to derive the precise dimensions of the Fe_2O_3 nanorods, the lattice distance, and the g-C_3N_4 thicknesses. Bare Fe_2O_3 nanorods were ~60 nm in diameter

[Fig. 2(a)]. All Fe_2O_3 nanorods had a high aspect ratio (16.7 : 1), enhancing the surface area and thus active sites. The TEM images of g-C_3N_4 coated onto Fe_2O_3 [Fig. 2(b) to (d)] showed that the Fe_2O_3 nanorods were fully covered with g-C_3N_4. Furthermore, the g-C_3N_4 coat was <10 nm in thickness, but this varied slightly because of yield effects during thermal evaporation. If g-C_3N_4 precursors are loaded onto Fe_2O_3 films to different extents under atmospheric conditions, g-C_3N_4 production levels will vary, affecting the final coating layers. Fast Fourier Transform (FFT) [Fig. 2(e)] revealed that the interplanar spacing in Fe_2O_3 was 0.37 nm, corresponding to the lattice distance of the (012) plane for Fe_2O_3. Thus, our heterostructures of 1D Fe_2O_3 nanorods covered with g-C_3N_4 sheets, were successfully synthesized using the relatively low pressurized solvothermal method which have shown good catalytic performance due to efficient separation of charge carriers right at the interface between g-C_3N_4 and Fe_2O_3, resulting in enhanced electron movements along with 1D structures.

3.2 Characterization

Fig. 3(a) shows the Fe_2O_3 crystallinities of bare Fe_2O_3 and all of the prepared heterostructures using XRD analysis. Distinct Fe_2O_3 peaks are evident at 24.10, 33.08, 35.61 and 51.58°, corresponding to the (012), (104), (110), and (116) planes, respectively. The structure was hematite in nature (α-Fe_2O_3), as indicated by the JCPDS 01-084-0306 criteria, and the Fe_2O_3 lattice constants were $a = b = 4.69$ Å and $c = 13.83$ Å in the hexagonal structure. In the heterostructures, the sharp diffraction peaks indicated high-level Fe_2O_3 crystallinity and no impurity peak was appeared. The photoanode films were subjected to XRD and the diffraction peaks of the SnO_2 phase were thus observed (JCPDS no. 01-070-6995). The peaks for bulk g-C_3N_4 were observed to be (100) and (002) planes at 13° and 27°, respectively as shown in Fig. S4(b).† The initial peak for (100) plane was presented as the in-plane structural packing of triazine and the other intense peak for (002) plane was presented as the inter-planar spacing from aromatic group of g-C_3N_4.[14] However, g-C_3N_4 was not detected by XRD; overall, the g-C_3N_4 loadings were relatively low in heterostructure films. Raman spectroscopy was used to identify characteristic Fe_2O_3 peaks [Fig. 3(b)]. Principal peaks were evident at 217, 290, 407, 493, and 603 cm^{-1}, corresponding to the A_{1g}, E_{1g}, E_{1g}, A_{1g}, and E_{1g} modes, respectively.[46] For the case of bulk g-C_3N_4, the intense peaks were observed at 483.2, 708.6, 754.4, 976.9, 1235.9, 1313.9 and 1566.8 cm^{-1}, relating g-C_3N_4 groups as shown in Fig. S4(c).† Among the Raman peaks, the peaks for g-C_3N_4 structures were presented at 483.2, 754.4, 976.9 and 1313.9 cm^{-1}.[47] Moreover, the initial peak of 708.6 cm^{-1} was presented to be the *s*-triazine ring for g-C_3N_4 group. The peaks at 1235.9 and 1566.8 cm^{-1} are observed to be the disorder in graphite structure and stretching mode in C=N bonding structure, respectively.[48] However, again, g-C_3N_4 peaks were not detected because the g-C_3N_4 levels were low. Therefore, we used FT-IR to analyze the molecular compositions. In Fig. 3(c), the Fe_2O_3 peaks at 534 and 467 cm^{-1} correspond to stretching vibrations of the Fe–O bonds of FeO_6 octahedral and FeO_4 tetrahedral sites, respectively.[49] The bulk g-C_3N_4 was compared for its specific g-C_3N_4 patterns with ones for the heterostructures. The principal g-C_3N_4 peaks range from 1700 to 1200 cm^{-1}, corresponding to stretching vibrations of tri-*s*-triazine in the heterocyclic rings. In detail, the bands at 1448, 1370 and 1250 cm^{-1} correspond to aromatic C–N stretching vibrations.[50] Furthermore, the band at 816 cm^{-1} corresponds to the *s*-triazine unit of the graphite-like sp^2 bonding state. It is clearly confirmed that all g-C_3N_4 related peaks are shown in the as-fabricated heterostructures as well as bulk g-C_3N_4. Moreover, broad peaks at 3500–3000 cm^{-1} corresponded to N–H and O–H stretching vibrations caused by surface adsorption of H_2O.[51] Thus, we have confirmed the presence of g-C_3N_4 on Fe_2O_3.

To explore the relationship between the C and N elements and Fe, XPS was performed as shown in Fig. 4. The typical Fe 2p spectrum of bare Fe_2O_3 features two different peaks (Fe $2p_{1/2}$ and Fe $2p_{3/2}$) of binding energies 709.0 eV and 722.8 eV, respectively [Fig. 4(a)]. Between these peaks, a satellite Fe^{3+} peak is apparent. In the O 1s spectrum, bare Fe_2O_3 exhibits principal peaks at 528.0 eV, 528.2 eV, 529.9 eV, and 531.5 eV, which are mainly attributable to Fe–O bonding, lattice oxygen, the hydroxyl group, and surface-absorbed H_2O, respectively [Fig. 4(b)].[44] Fig. 4(c) shows the 0.75g-C_3N_4@Fe_2O_3 Fe 2p spectrum (peaks at 708.9 eV for Fe $2p_{1/2}$ and 722.7 eV for Fe $2p_{3/2}$) of the g-C_3N_4 coating. Fig. 4(d) shows similarly broad principal peaks at 528.0 eV, 529.0 eV, 529.7 eV, and 531.0 eV.[52] As g-C_3N_4 coated Fe_2O_3, C 1s and N 1s spectra were detected. The C 1s spectrum exhibits binding energies at 286.5, 285.4, 284.3, and 282.7 eV, corresponding to sp^2-hybridized carbon in the tri-*s*-triazine rings C=O, C–O, C–C and C=C bonding, respectively [Fig. 4(e)].[53,54] In the N 1s spectrum [Fig. 4(f)], the binding energy peaks at 396.1, 397.7, and 399.6 eV correspond to sp^2-hybridized nitrogen (C–N=C), tertiary nitrogen [N–$(C)_3$], and –NH_2 bonding, respectively, and were unique to the g-C_3N_4 moieties.[41] Fig. 4(g) and (h) showed the C 1s and N 1s spectrums of bulk g-C_3N_4 for comparison, respectively. The bulk g-C_3N_4 shows three different peak positions at 288.5, 287.2 and 283.9 eV in C 1s spectrum. The peaks for 288.5 eV, 287.2 eV are for sp^2-hybridized bonding of N–C=N in aromatic and C–N bonds in carbon species of bulk g-C_3N_4, respectively. The peak for 283.9 eV is assigned to the carbon contamination during the samples preparation. In N 1s spectrum, the main peak of 397.7 eV is ascribed to C=N–C bonding while the peak of 398.5 eV is ascribed to N–$(C)_3$ bonded group. The weaker peaks of 400.2 and 403.6 eV are attributed to amino functional groups in aromatic rings of g-C_3N_4 and π-excitation which is positively charged localization in heterocycles, respectively.[60] When the 0.75 g of melamine is coated onto Fe_2O_3 film to convert into g-C_3N_4 layer, the amounts of coating layer are considerably lower than that of bulk g-C_3N_4. Thus, the carbon and nitrogen spectrums of 0.75g-C_3N_4@Fe_2O_3 showed relatively low intensity compared to that of bulk g-C_3N_4 even though it represented the carbon and nitrogen-related bonding as shown in Fig. 4(e) and (f). Therefore, that obvious peak shift for C=N–C and N–$(C)_3$ at 397.7 and 398.5 eV suggest the chemically formed heterojunctions between Fe_2O_3 and g-C_3N_4.

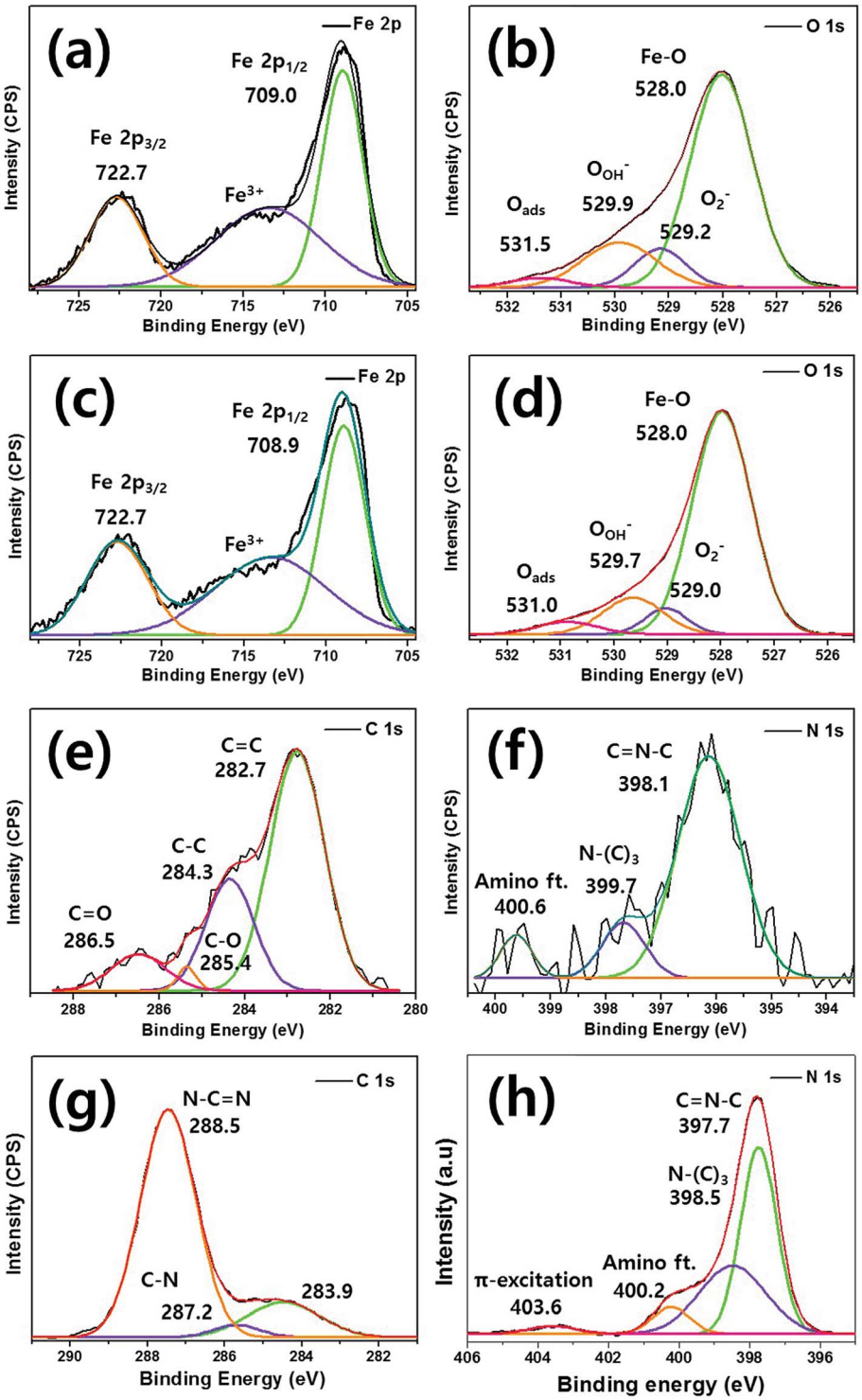

Fig. 4 The chemical binding energies evident on bare Fe_2O_3 spectra of (a) Fe 2p and (b) O 1s. The 0.75g-C_3N_4@Fe_2O_3 spectra of (c) Fe 2p, (d) O 1s, (e) C 1s, and (f) N 1s and bulk g-C_3N_4 spectra of (g) C 1s and (h) N 1s based on X-ray photoelectron spectroscopy (XPS) analysis-fitting results.

3.3 Optical properties

To study the absorbance ranges and band gap energies of the prepared films, the optical absorbance was measured from 300 to 800 nm as shown in Fig. 5(a). Bare Fe_2O_3 exhibited a slow absorption edge around 550 nm while the bulk g-C_3N_4 showed a steep absorption edge around 430 nm. However, when g-C_3N_4 was coated onto Fe_2O_3 films in different amounts, notable peaks were observed around 550 nm and the absorption edges became steeper because of g-C_3N_4 coating. Thus, all g-C_3N_4@Fe_2O_3 films exhibited higher absorption intensities than that of bare Fe_2O_3 during the entire UV-visible region, suggesting the enhancement of the absorption ability under

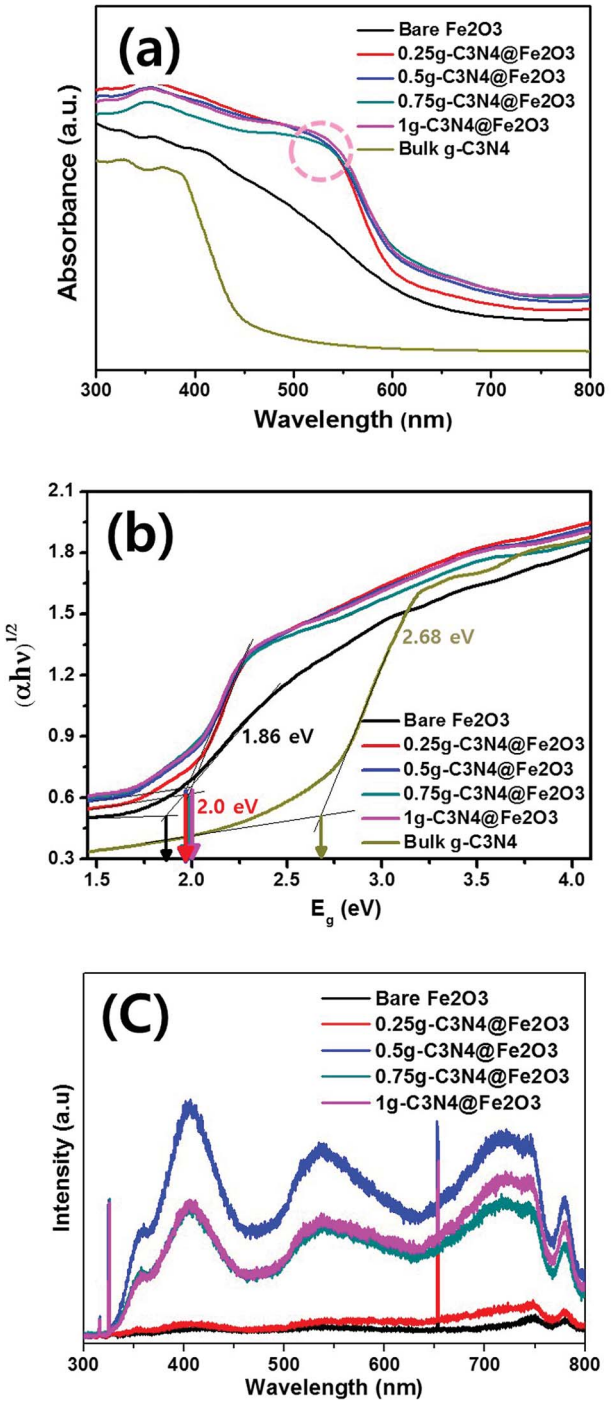

Fig. 5 Band gap energy measurement results based on (a) optical absorbances, (b) calculated absorbances, and (c) photoluminescence for bare Fe_2O_3, 0.25g-C_3N_4@Fe_2O_3, 0.5g-C_3N_4@Fe_2O_3, 0.75g-C_3N_4@Fe_2O_3, 1g-C_3N_4@Fe_2O_3 and bulk g-C_3N_4.

illumination. The absorbance was calculated into band gap energies using the Kubelka–Munk function in Fig. 5(b). Although there is a difference in the absorption edge, all g-C_3N_4@Fe_2O_3 films exhibited similar band gap energies of 2.0 eV. When the g-C_3N_4 is coated onto Fe_2O_3 nanorod film, the band gap difference has occurred for sure, compared to that of bare Fe_2O_3 film of 1.86 eV. Based on calculated band gap of bulk g-C_3N_4, it exhibited 2.68 eV of band gap energy. Therefore, as-prepared heterostructure films provided the higher absorption intensity, with extending its utilization of light irradiation, compared to that of bare Fe_2O_3, confirming successful formation of heterostructure film.

Fig. 5(c) shows PL spectra exploring recombination or transfer of photogenerated electrons and hole pairs between Fe_2O_3 and g-C_3N_4. Typically, large (>70 nm) nanomaterials do not exhibit PL since optical transition is not possible[55] and our Fe_2O_3 nanorods also did not show any significant emission peaks. In other words, 0.25g-C_3N_4@Fe_2O_3 film also showed almost no PL emission peak possibly due to small amounts of g-C_3N_4 loading on bare Fe_2O_3. The 0.5g-C_3N_4@Fe_2O_3 showed the highest PL intensity among the samples because of the fast charge recombination. On the other hand, the 1g and 0.75g-C_3N_4@Fe_2O_3 were observed with similar PL intensity while 0.75g-C_3N_4@Fe_2O_3 showed lower intensity than that of 1g-C_3N_4@Fe_2O_3. This means that 0.75g-C_3N_4@Fe_2O_3 makes good heterojunction of interfaces, reflecting effective separation of electron and hole pairs. Furthermore, the bulk g-C_3N_4 was measured for comparison as shown in Fig. S4(d).† As a result, it showed high PL intensity at 423 nm of wavelength, attributing to fast recombination rate of charge carriers in bulky structures. Of all the photoanodes, 0.75g-C_3N_4@Fe_2O_3 associated with rapid electron movement and thus enhancement of PEC-mediated water splitting and photocatalytic performance.

3.4 Photoelectrochemical analysis

We used PEC analysis to evaluate photoresponses in the presence of 0.5 M Na_2SO_4 under visible illumination. Fig. 6(a) shows the transient photocurrents during light-chopping. The overall on–off cycles of all films are presented in Fig. S5(a).† During the on–off cycles, when the light was on, the film photoresponses were rapid. In the curves, the strong spikes in the light-on phases reflect electron–hole recombination on the surfaces during photocatalytic reactions. When recombination is slow, the spike peak is broad and the electron–hole combination exhibits a longer lifetime than that of the bare Fe_2O_3 film because of effective electron/hole separation during irradiation.[56] Of the various hybrid films, the 0.75g-C_3N_4@Fe_2O_3 film exhibited slow and broad recombination, associated with a higher photocurrent (1.0 mA) than the other samples. Bare Fe_2O_3 exhibited almost no current (*ca.* 0.005 mA), whereas stepwise g-C_3N_4 coating increased the photocurrent proportionately (to 0.25g, 0.5g and 1g C_3N_4 values of 0.02, 0.06 and 0.09 mA, respectively). The photocurrent for bulk g-C_3N_4 was measured to be 0.04 mA under the same condition, exhibiting similar photocurrent with bare Fe_2O_3 and 0.25g-C_3N_4@Fe_2O_3 film. As expected, the 0.75g-C_3N_4@Fe_2O_3 film exhibited the highest photocurrent because charge separation was effective; recombination was low after the light came on. Surprisingly, the current was about 200-fold that of the bare Fe_2O_3 film because of optimization of the g-C_3N_4 coating layer, suggesting that photogenerated electrons and hole pairs separated effectively

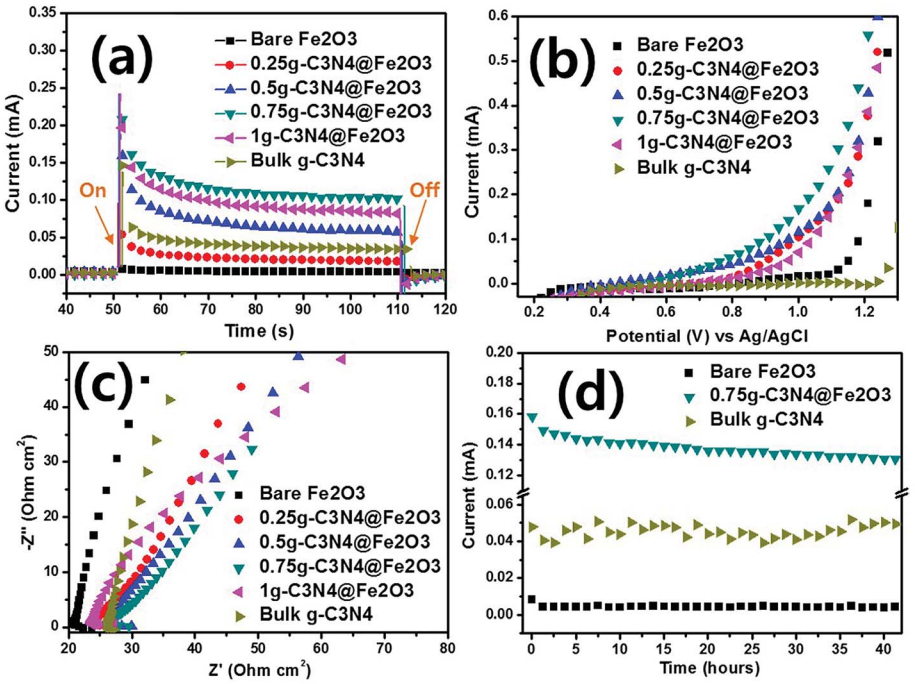

Fig. 6 (a) Photoresponse measurements of transient photocurrents with on/off light. (b) Linear sweep voltammetry (LSV) data. (c) Electrical impedance spectroscopy (EIS) data derived using bare Fe_2O_3, 0.25g-C_3N_4@Fe_2O_3, 0.5g-C_3N_4@Fe_2O_3, 0.75g-C_3N_4@Fe_2O_3, 1g-C_3N_4@Fe_2O_3 and bulk g-C_3N_4. (d) The photoresponse stability of bare Fe_2O_3 *vs.* 0.75g-C_3N_4@Fe_2O_3 *vs.* and bulk g-C_3N_4 under visible irradiation.

due to good formation of interface between g-C_3N_4 and Fe_2O_3 in heterojunctions.

The photocurrent *versus* applied potential curves of bare Fe_2O_3, and the various heterostructures, were assessed using LSV under identical conditions. In the dark, no photoresponse attributable to hybridization was apparent [dashed line in Fig. S5(b)†].[57] In the light [Fig. 6(b)], the bare Fe_2O_3 and bulk g-C_3N_4 films produced almost no photocurrent according to

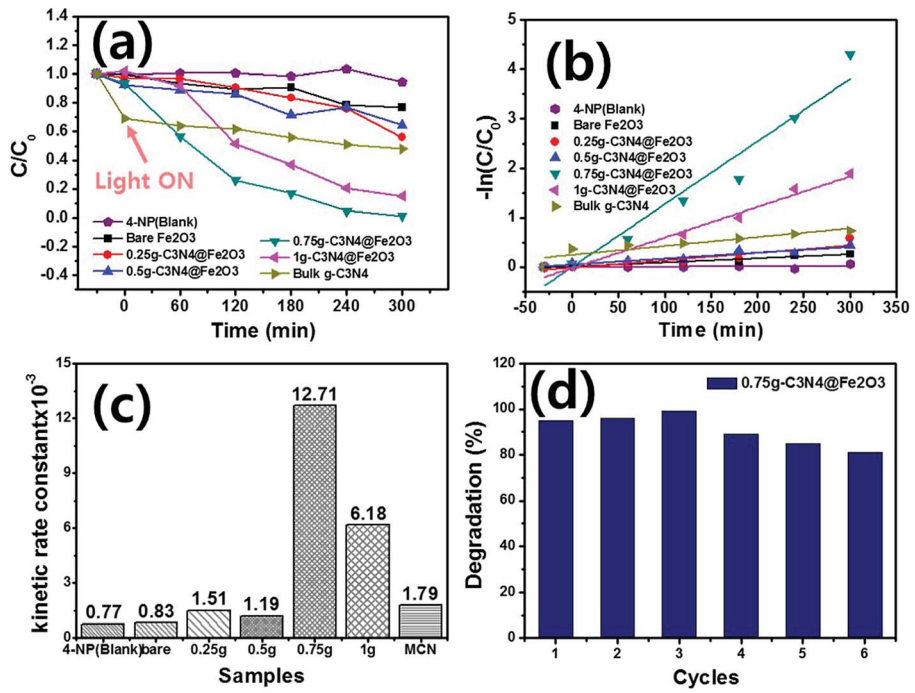

Fig. 7 Photocatalytic degradation of 4-nitrophenol (4-NP). (a) Relative absorbances. (b) Logarithms of absorbances. (c) Kinetic rate constants of 4-NP (blank), bare Fe_2O_3, 0.25g-C_3N_4@Fe_2O_3, 0.5g-C_3N_4@Fe_2O_3, 0.75g-C_3N_4@Fe_2O_3, 1g-C_3N_4@Fe_2O_3 and bulk g-C_3N_4. (d) Reusability testing of 0.75g-C_3N_4@Fe_2O_3 under visible irradiation.

applied potential *versus* Ag/AgCl. In contrast, the various hybrid films exhibited photocurrents. The photoresponses of the 0.25g, 0.5g, and 1g-C_3N_4@Fe_2O_3 films were similar. The 0.75g-C_3N_4@Fe_2O_3 film evidenced the highest performance at 1 V *versus* Ag/AgCl. Therefore, the g-C_3N_4 coat formed a useful heterojunction with Fe_2O_3, reducing the recombination rate of the charge carriers.

EIS was used to measure charge transfers from the g-C_3N_4@Fe_2O_3/electrolyte interface. In the dark, all films tested (bare Fe_2O_3 and the various heterostructures) exhibited higher impedances than in the light [Fig. S5(c)†]. Fig. 6(c) shows the impedances of all samples, where that of bare Fe_2O_3 was highest. In the light, the electrons and holes created favor the separation of charge carriers, reducing interface resistance. All g-C_3N_4-coated films exhibited smaller arc curves than that of bare Fe_2O_3 and bulk g-C_3N_4. The Fe_2O_3 and g-C_3N_4 themselves only, are difficult to overcome the high recombination rate, resulting in high resistance between photocatalysts and electrolyte. Of all films, the 0.75g-C_3N_4@Fe_2O_3 film exhibited the smallest arc radius, suggesting that the heterostructure can effectively support transfer of the abundant electrons, minimizing surface recombination losses and further improving photocatalytic activities.

After PEC evaluation, we performed stability testing under the conditions shown in Fig. 6(d). Only bare Fe_2O_3 and 0.75g-C_3N_4@Fe_2O_3 were subjected to such testing. The latter film remained photoresponsive to 40 h and bare Fe_2O_3 was not photoresponsive. The stability of bulk g-C_3N_4 was also conducted for comparison under visible light and it showed unstable photocurrent of 0.04 mA. Despite a slight decrease in the 0.75g-C_3N_4@Fe_2O_3 photocurrent over time, this remained higher than that of Fe_2O_3. Therefore, the 0.75g-C_3N_4@Fe_2O_3 film was an optimized heterostructure featuring Fe_2O_3 and g-C_3N_4 coating layers.

3.5 Photocatalytic degradation and scavenger test

Photocatalytic degradation of 4-NP by g-C_3N_4@Fe_2O_3 films under visible light was examined. In order to facilitate photocatalytic reactions, 0.5 mL of H_2O_2 was added into 4-NP solution since the 4-NP solution was not degraded at all without presence of H_2O_2 during photodegradation evaluation, as shown in Fig. S6.† Fig. 7(a) illustrates the relative absorbance of all samples by the extent of 4-NP degradation over time. The blank was a pure 4-NP solution (thus, assessing spontaneous degradation). Degradation commenced in the dark for 30 min to confirm that adsorption was stable. As a result, few adsorption difference with negligible adsorption properties were observed under a dark state. When the visible light is illuminated, the catalysts started to remove the 4-NP organic pollutant with increasing time. Of the various films, the 0.75g-C_3N_4@Fe_2O_3 film exhibited the highest extent of degradation, removing all 4-NP by 300 min. The 1g-C_3N_4@Fe_2O_3 film also afforded rapid degradation because of the extensive g-C_3N_4 coating. However, the thick coating inhibited rapid transfer of solar energy into the catalyst; thus, the 0.75g-C_3N_4@Fe_2O_3 film was more effective than the 1g-C_3N_4@Fe_2O_3 film. In contrast, the 0.5g and 0.25g-C_3N_4@Fe_2O_3 films exhibited activities similar to that of bare Fe_2O_3 because the g-C_3N_4 coatings were thin.[58] Each absorbance graph monitored the 4-NP absorption peak at 325 nm (Fig. S7†). For comparison, the bulk g-C_3N_4 was performed for the photocatalytic degradation using 4-NP, exhibiting higher adsorption under the dark condition to be ~31% but showing almost no degradation for 4-NP. To study the kinetic rate, the 4-NP levels were log-transformed and plotted [Fig. 7(b)]. The degradation followed a pseudo first-order equation [the Langmuir–Hinshelwood (L–H) mechanism],[5] mathematically denoted as follows:

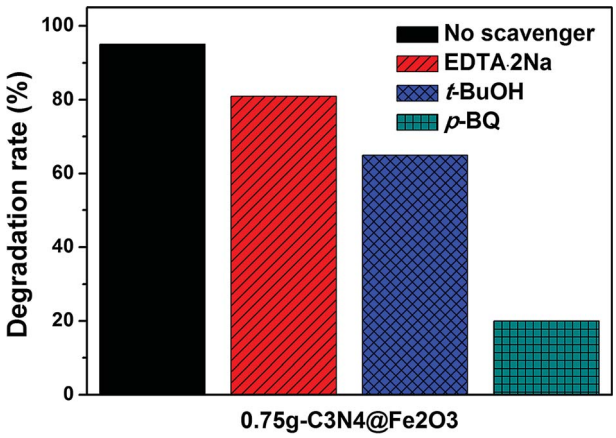

Fig. 8 The scavenger test of 0.75g-C_3N_4@Fe_2O_3 without radical trapping, EDTA·2Na, *t*-BuOH and *p*-BQ under visible irradiation.

$$-\ln(C/C_o) = kt \quad (1)$$

Based on eqn (1), plots of $-\ln(C/C_o)$ *versus* time were linear; k was the kinetic rate constant (min^{-1}) of catalytic degradation. The correlation coefficient R is shown in Table 1. The kinetic rate constant for 0.75g-C_3N_4@Fe_2O_3 (12.71×10^{-3} min^{-1}) was ~15-fold higher than that of bare Fe_2O_3 (0.83×10^{-3} min^{-1}) [Fig. 7(c)]. The k values for 4-NP degradation by 0.25g, 0.5g, 1g-C_3N_4@Fe_2O_3 and bulk g-C_3N_4 were 0.77×10^{-3}, 1.51×10^{-3}, 1.19×10^{-3}, 6.18×10^{-3} min^{-1} and 1.79×10^{-3} min^{-1}, respectively. The reason for enhancement of photocatalytic degradation going from bare Fe_2O_3 and bulk g-C_3N_4 to g-C_3N_4@Fe_2O_3 heterostructure films, could be explained by the photoresponse result shown in Fig. 6(d). As shown in the figure, the heterojunction formed between g-C_3N_4 and Fe_2O_3 coated with g-C_3N_4, shows higher current than those of bare Fe_2O_3 and

Table 1 The kinetic constants of photocatalytic degradation

	k min^{-1}	R^2
4-Nitrophenol	0.77×10^{-3}	0.775685
Bare Fe_2O_3	0.83×10^{-3}	0.90604
0.25g-C_3N_4@Fe_2O_3	1.51×10^{-3}	0.79317
0.5g-C_3N_4@Fe_2O_3	1.19×10^{-3}	0.87725
0.75g-C_3N_4@Fe_2O_3	12.71×10^{-3}	0.9439
1g-C_3N_4@Fe_2O_3	6.18×10^{-3}	0.95215
Bulk g-C_3N_4	1.79×10^{-3}	0.78454

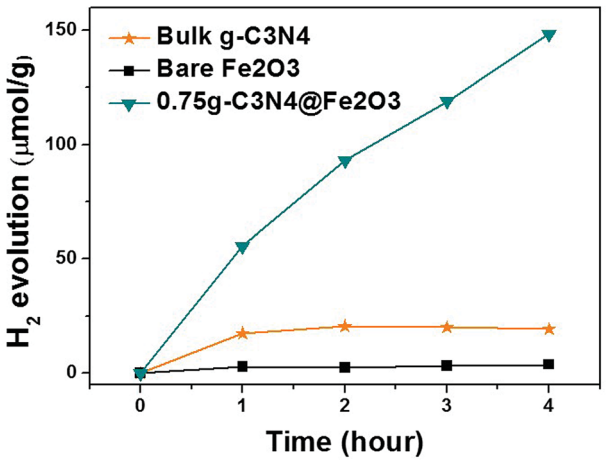

Fig. 9 Hydrogen evolution triggered by bulk g-C_3N_4 from melamine precursors, by bare Fe_2O_3, and by 0.75g-C_3N_4@Fe_2O_3 using Pt as the co-catalyst under visible irradiation.

bulk g-C_3N_4, due to the efficient separation of charge carriers as well as reducing recombination rates at its interface. Consequently, g-C_3N_4@Fe_2O_3 heterostructure film showed better photodegradation ability with higher kinetic rate constant compared to those of bare Fe_2O_3 and bulk g-C_3N_4 film. To explore the reusability of 0.75g-C_3N_4@Fe_2O_3 (which exhibited excellent performance), we recycled the film six times [Fig. 7(d)]. The extent of degradation was >80% after each recycle, indicating good reusability. Furthermore, new 0.75g-C_3N_4@Fe_2O_3 film was prepared to confirm the repeatability in photodegradation ability under the same condition as shown in Fig. S8.† As a result, it shows similar kinetic rate constant with its error range less than 10%. The 0.75g-C_3N_4@Fe_2O_3 film exhibited remarkable photocatalytic degradation of 4-NP, attributable to rapid separation of charge carriers at the g-C_3N_4@Fe_2O_3 interface and thus promoting photo-oxidation to successfully remove the organic pollutant using a direct z-scheme pathway.

Prior to suggesting possible mechanism of these heterostructures, scavenger tests shown in Fig. 8, are performed to study the photocatalytic reaction in detail. For the photocatalytic activity, there are main free radicals as active species which are hole (h^+), hydroxyl radical ($\cdot OH$) and superoxide radical ($\cdot O_2^-$). To observe the radical trapping performances, 0.75g-C_3N_4@Fe_2O_3 film was used under light illumination. Here, EDTA·2Na was used to capture a h^+, *tert*-butanol (*t*-buOH) was used for $\cdot OH$ and *p*-benzoquinone (*p*-BQ) was used for $\cdot O_2^-$. When the photodegradation rate of 0.75g-C_3N_4@Fe_2O_3 film itself was approximately 95%, EDTA·2Na and *t*-buOH scavengers showed 81% and 65% degradation rates, respectively, suggesting h^+ and $\cdot OH$ are not a crucial role in this photocatalytic activity. In contrast, *p*-BQ scavenger exhibited a significant decrease in 4-NP degradation of 20%. Therefore, it was confirmed that O_2^- is found to be the main active species that works for 0.75g-C_3N_4@Fe_2O_3 film.

3.6 Hydrogen evolution and its possible mechanism

We evaluated hydrogen evolution to further explore the photocatalytic activities of the films under visible illumination. Fig. 9 illustrates H_2 production by bulk g-C_3N_4, bare Fe_2O_3, and 0.75g-C_3N_4@Fe_2O_3 over 4 h. Only the 0.75g-C_3N_4@Fe_2O_3 film effectively evolved H_2; its performance in this context was excellent. Bulk g-C_3N_4, made using melamine as precursor and bare Fe_2O_3, evolved 4.79 μmol h^{-1} g^{-1} and 0.94 μmol h^{-1} g^{-1} H_2, respectively. However, the figure for 0.75g-C_3N_4@Fe_2O_3 was 37.06 μmol h^{-1} g^{-1}, almost 39-fold that of bare Fe_2O_3. Generally, Fe_2O_3 does not produce H_2 because the conduction level of Fe_2O_3 is just below the proton reduction potential.[59] Even when Pt is added to bare Fe_2O_3 (as a co-catalyst), H_2 evolution remains

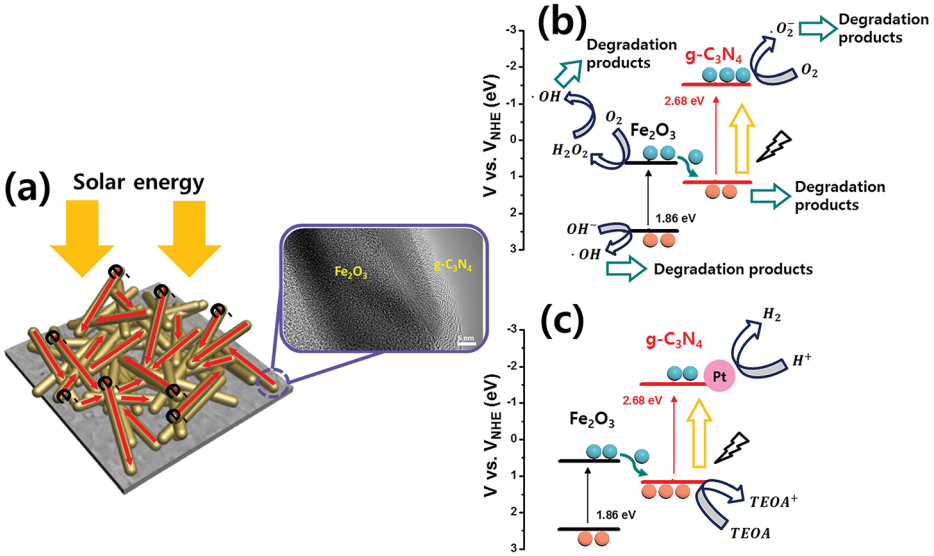

Fig. 10 The direct z-scheme mechanism of 0.75g-C_3N_4@Fe_2O_3 heterostructures showing (a) a graphical schematics, bandgap energy diagrams for (b) photocatalytic degradation and (c) H_2 evolution.

very low because of rapid recombination of charge carriers. The 0.75g-C_3N_4@Fe_2O_3 film forms the optimized interface between Fe_2O_3 and g-C_3N_4 for heterojunction, facilitating electron movements due to reducing its recombination rates of charge carriers. Therefore, these results show that the improvement in several properties, like accelerating electron transfer which can subsequently improve the possibility of photoresponse, can be started through 1D structure.[60,61]

Based on these results, the mechanisms of g-C_3N_4@Fe_2O_3 heterostructures are shown in Fig. 10. Under solar light irradiation, electrons that are generated are transferred elsewhere by the 1D Fe_2O_3 nanorods, accompanied by recombination losses attributable to the g-C_3N_4 coating. The heterostructures can be used to degrade organic pollutants, or to produce gaseous fuels. In order to prove Z-type mechanism from the photocatalytic mechanism, the schematics of band diagram for the heterostructure in Fig. 10, can be used. As shown in Fig. 10, the electrons from the valence band of Fe_2O_3 is excited to the conduction band of Fe_2O_3 under the light as they are transferred into the valence band of g-C_3N_4, for its band edge being very close for the electron movement. Again, the excited electrons in g-C_3N_4 structure react with oxygen, producing superoxide radical to degrade 4-NP on g-C_3N_4 surface. To prove this point in terms of band edge between Fe_2O_3 and g-C_3N_4, we have measured the valence band of each material using XPS analysis (Fig. S9(a)–(c)†) as well as energy band gap from optical absorbance analysis. As a result, we had measured valence band for g-C_3N_4 to be 1.13 eV while the conduction band for Fe_2O_3 was estimated to be 0.62 eV based on the energy band gap measurement (Fig. 5), proving fairly close band edge between Fe_2O_3 and g-C_3N_4 with Z-type mechanism. Fig. 10(b) shows the 4-NP degradation mechanism. Under visible light, photogenerated electrons from the Fe_2O_3 conduction band are transferred to the valence band of g-C_3N_4, exciting other photogenerated electrons into the g-C_3N_4 conduction band. The resulting holes in Fe_2O_3 react with H_2O and OH^- to produce ·OH radicals on the surface of Fe_2O_3. Moreover, the photogenerated electrons in Fe_2O_3 react with oxygen molecules at the surface of Fe_2O_3 to produce H_2O_2. ·OH radicals facilitate the removal of 4-NP organic pollutant. Also, electrons from the g-C_3N_4 conduction level react with oxygen on the surface of g-C_3N_4, producing $\cdot O_2^-$ and allowing 4-NP to be degraded to water.[44] From the scavenger test, the main active species in this reaction system is observed to be $\cdot O_2^-$ species.[62] When H_2 is evolved by heterostructures, the direct z-scheme can be used to explain the mechanism detailed previously[63] [Fig. 10(c)]. When producing H_2 using Fe_2O_3 and g-C_3N_4, TEOA features hole capture, accelerating electron transfer throughout Pt, and, finally, H_2 production. Therefore, the g-C_3N_4@Fe_2O_3 heterostructures feature separation of charge carriers at the interface, effectively enriching photocatalytic activities and thus allowing 4-NP degradation and H_2 evolution.

4. Conclusion

We successfully synthesized 1D g-C_3N_4@Fe_2O_3 nanorod/film heterostructures using a solvothermal method, to align the Fe_2O_3 nanorod film and thermal evaporation to ensure uniform g-C_3N_4 coating of the film. The thickness of the g-C_3N_4 coat varied morphologically by the amount of g-C_3N_4 added compared to bare Fe_2O_3 All samples exhibited properties on XRD, FT-IR, Raman spectroscopy, and XPS analysis compatible with reliable formation of g-C_3N_4@Fe_2O_3 heterostructures. Bare Fe_2O_3 exhibited poor electron transfer because of rapid recombination of charge carriers. The g-C_3N_4 coating of Fe_2O_3 films increased the photoresponse performance, as revealed by transient photocurrent, LSV, and EIS measurements. Furthermore, the 4-NP-degrading photocatalytic activity of g-C_3N_4 coated Fe_2O_3 films under visible light was much more rapid than that afforded by bare Fe_2O_3. Of the various heterostructures, the 0.75g-C_3N_4@Fe_2O_3 film exhibited excellent 4-NP degradation for up to 300 min, with a kinetic rate constant of 12.71×10^{-3} min^{-1}, along with stable recyclability. We also evaluated H_2 evolution caused by photocatalytic activity during 4 h of irradiation with visible light. The 0.75g-C_3N_4@Fe_2O_3 film produced 37.06 μmol h^{-1} g^{-1} of H_2, 39-fold higher than that produced by bare Fe_2O_3, suggesting that charge separation was efficient and that accumulated electrons accelerated H_2 evolution *via* a direct z-scheme mechanism. Heterostructures composed of g-C_3N_4 coated onto 1D Fe_2O_3 nanorods exhibited remarkable photocatalytic activity under visible illumination; electron transfer through 1D structure and charge separation were highly efficient.

Conflicts of interest

There are no conflicts to declare.

Acknowledgements

This work was supported by a National Research Foundation of Korea (NRF) grant funded by the Korean government (Ministry of Education) (no. NRF-2016R1D1A1A02936936), the NRF grant funded by the Korean government (MEST) (no. NRF-2018R1A2A1A13078704) and supported by the Human Resources Development Program (grant no. 20174030201830) of the Korea Institute of Energy Technology Evaluation and Planning (KETEP) funded by the Korean Ministry of Trade, Industry, and Energy. The English in this document has been checked by at least two professional editors, both native speakers of English.

References

1 J. Ran, M. Jaroniec and S. Z. Qiao, *Adv. Mater.*, 2018, **30**, 1–31.
2 J. Potočnik, *Scinece*, 2007, **315**, 810.
3 J. Gu, J. Yan, Z. Chen, H. Ji, Y. Song, Y. Fan, H. Xu and H. Li, *Dalton Trans.*, 2017, **46**, 11250–11258.
4 A. Boudjemaa, A. Rebahi, B. Terfassa, R. Chebout, T. Mokrani, K. Bachari and N. J. Coville, *Sol. Energy Mater. Sol. Cells*, 2015, **140**, 405–411.
5 X. Liu, L. Zhao, H. Lai, S. Li and Z. Yi, *J. Chem. Technol. Biotechnol.*, 2017, **92**, 2417–2424.

6 Y. H. Li, Y. Wang, L. R. Zheng, H. J. Zhao, H. G. Yang and C. Li, *Appl. Catal., B*, 2017, **209**, 247–252.
7 N. A. Romero and D. A. Nicewicz, *Chem. Rev.*, 2016, **116**, 10075–10166.
8 S. Peiris, J. McMurtrie and H.-Y. Zhu, *Catal. Sci. Technol.*, 2016, **6**, 320–338.
9 H. Hou, F. Gao, L. Wang, M. Shang, Z. Yang, J. Zheng and W. Yang, *J. Mater. Chem. A*, 2016, **4**, 6276–6281.
10 A. Ali and W.-C. Oh, *J. Korean Ceram. Soc.*, 2017, **54**, 308–313.
11 S. Li, X. Shen, J. Liu and L. Zhang, *Environ. Sci.: Nano*, 2017, **4**, 1155–1167.
12 S. Li, S. Hu, W. Jiang, Y. Liu, J. Liu and Z. Wang, *J. Colloid Interface Sci.*, 2017, **501**, 156–163.
13 S. Li, S. Hu, W. Jiang, Y. Liu, Y. Zhou, Y. Liu and L. Mo, *J. Colloid Interface Sci.*, 2018, **521**, 42–49.
14 S. Ye, R. Wang, M.-Z. Wu and Y.-P. Yuan, *Appl. Surf. Sci.*, 2015, **358**, 15–27.
15 A. Kudo and Y. Miseki, *Chem. Soc. Rev.*, 2009, **38**, 253–278.
16 L. Zhang and M. Jaroniec, *Appl. Surf. Sci.*, 2018, **430**, 2–17.
17 J. Zhang, G. Xiao, F.-X. Xiao and B. Liu, *Mater. Chem. Front.*, 2017, **1**, 231–250.
18 S. Li, S. Hu, W. Jiang, Y. Liu, Y. Liu, Y. Zhou, L. Mo and J. Liu, *Beilstein J. Nanotechnol.*, 2018, **9**, 1308–1316.
19 D. M. Arias-Rotondo and J. K. McCusker, *Chem. Soc. Rev.*, 2016, **45**, 5803–5820.
20 J. Low, C. Jiang, B. Cheng, S. Wageh, A. A. Al-Ghamdi and J. Yu, *Small Methods*, 2017, **1**, 1700080.
21 P. Zhou, J. Yu and M. Jaroniec, *Adv. Mater.*, 2014, **26**, 4920–4935.
22 H. Li, W. Tu, Y. Zhou and Z. Zou, *Adv. Sci.*, 2016, **3**, 1500389.
23 H. Katsumata, T. Sakai, T. Suzuki and S. Kaneco, *Ind. Eng. Chem. Res.*, 2014, **53**, 8018–8025.
24 J. C. Wang, L. Zhang, W. X. Fang, J. Ren, Y. Y. Li, H. C. Yao, J. S. Wang and Z. J. Li, *ACS Appl. Mater. Interfaces*, 2015, **7**, 8631–8639.
25 J. Zhang, Y. Hu, X. Jiang, S. Chen, S. Meng and X. Fu, *J. Hazard. Mater.*, 2014, **280**, 713–722.
26 S. Kang, R. C. Pawar, T. J. Park, J. G. Kim, S.-H. Ahn and C. S. Lee, *J. Korean Ceram. Soc.*, 2016, **53**, 393–399.
27 M. Zhang, Y. Duan, H. Jia, F. Wang, L. Wang, Z. Su and C. Wang, *Catal. Sci. Technol.*, 2017, **7**, 452–458.
28 Y. Liao, S. Zhu, J. Ma, Z. Sun, C. Yin, C. Zhu, X. Lou and D. Zhang, *ChemCatChem*, 2014, **6**, 3419–3425.
29 K. S. Lakhi, D. H. Park, K. Al-Bahily, W. Cha, B. Viswanathan, J. H. Choy and A. Vinu, *Chem. Soc. Rev.*, 2017, **46**, 72–101.
30 Y. Wang, J. Sun, J. Li and X. Zhao, *Langmuir*, 2017, **33**, 4694–4701.
31 R. Cheng, L. Zhang, X. Fan, M. Wang, M. Li and J. Shi, *Carbon*, 2016, **101**, 62–70.
32 J. Yu, S. Wang, J. Low and W. Xiao, *Phys. Chem. Chem. Phys.*, 2013, **15**, 16883–16890.
33 B. Lin, C. Xue, X. Yan, G. Yang, G. Yang and B. Yang, *Appl. Surf. Sci.*, 2015, **357**, 346–355.
34 X.-j. Wang, C. Liu, X.-l. Li, F.-t. Li, Y.-p. Li, J. Zhao and R.-h. Liu, *Appl. Surf. Sci.*, 2017, **394**, 340–350.
35 S. Shen, S. A. Lindley, X. Chen and J. Z. Zhang, *Energy Environ. Sci.*, 2016, **9**, 2744–2775.
36 M. Imran, A. B. Yousaf, P. Kasak, A. Zeb and S. J. Zaidi, *J. Catal.*, 2017, **353**, 81–88.
37 J. Wang, J. L. Waters, P. Kung, S. M. Kim, J. T. Kelly, L. E. McNamara, N. I. Hammer, B. C. Pemberton, R. H. Schmehl, A. Gupta and S. Pan, *ACS Appl. Mater. Interfaces*, 2017, **9**, 381–390.
38 J. Wang, C. Qin, H. Wang, M. Chu, A. Zada, X. Zhang, J. Li, F. Raziq, Y. Qu and L. Jing, *Appl. Catal., B*, 2018, **221**, 459–466.
39 X. She, J. Wu, H. Xu, J. Zhong, Y. Wang, Y. Song, K. Nie, Y. Liu, Y. Yang, M.-T. F. Rodrigues, R. Vajtai, J. Lou, D. Du, H. Li and P. M. Ajayan, *Adv. Energy Mater.*, 2017, **7**, 1700025.
40 Y. Xu, S. Huang, M. Xie, Y. Li, H. Xu, L. Huang, Q. Zhang and H. Li, *RSC Adv.*, 2015, **5**, 95727–95735.
41 S. Hu, R. Jin, G. Lu, D. Liu and J. Gui, *RSC Adv.*, 2014, **4**, 24863.
42 H.-M. Xu, H.-C. Wang, Y. Shen, Y.-H. Lin and C.-W. Nan, *J. Appl. Phys.*, 2014, **116**, 174307.
43 L. Wang, X. Lu, C. Han, R. Lu, S. Yang and X. Song, *CrystEngComm*, 2014, **16**, 10618–10623.
44 H. Lin, Y. Liu, J. Deng, S. Xie, X. Zhao, J. Yang, K. Zhang, Z. Han and H. Dai, *J. Photochem. Photobiol., A*, 2017, **336**, 105–114.
45 J.-Y. Lee, M.-C. Tsai, P.-C. Chen, T.-T. Chen, K.-L. Chan, C.-Y. Lee and R.-K. Lee, *J. Phys. Chem. C*, 2015, **119**, 25754–25760.
46 Y. Li, X. Wei, B. Zhu, H. Wang, Y. Tang, T. C. Sum and X. Chen, *Nanoscale*, 2016, **8**, 11284–11290.
47 X. Wang, Y. Liang, W. An, J. Hu, Y. Zhu and W. Cui, *Appl. Catal., B*, 2017, **219**, 53–62.
48 P. V. Zinin, L.-C. Ming, S. K. Sharma, V. N. Khabashesku, X. Liu, S. Hong, S. Endo and T. Acosta, *Chem. Phys. Lett.*, 2009, **472**, 69–73.
49 T. Wang, Y. Li, L. Wang, C. Liu, S. Geng, X. Jia, F. Yang, L. Zhang, L. Liu, B. You, X. Ren and H. Yang, *RSC Adv.*, 2015, **5**, 60114–60120.
50 J. Di, J. Xia, S. Yin, H. Xu, L. Xu, Y. Xu, M. He and H. Li, *J. Mater. Chem. A*, 2014, **2**, 5340.
51 D. Chen, W. Wei, R. Wang, J. Zhu and L. Guo, *New J. Chem.*, 2012, **36**, 1589.
52 J. Wang, B. Feng, J. Su and L. Guo, *ACS Appl. Mater. Interfaces*, 2016, **8**, 23143–23150.
53 L. Liu, J. Wang, C. Wang and G. Wang, *Appl. Surf. Sci.*, 2016, **390**, 303–310.
54 Y. Yan, H. Tang, F. Wu, R. Wang and M. Pan, *Energies*, 2017, **10**, 1–13.
55 N. M. Abdul Rashid, C. Haw, W. Chiu, N. H. Khanis, A. Rohaizad, P. Khiew and S. Abdul Rahman, *CrystEngComm*, 2016, **18**, 4720–4732.
56 D. Li, W. Wang, D. Jiang, Y. Zheng and X. Li, *RSC Adv.*, 2015, **5**, 14374–14381.
57 Y. Liu, F.-Y. Su, Y.-X. Yu and W.-D. Zhang, *Int. J. Hydrogen Energy*, 2016, **41**, 7270–7279.
58 J. Zhang, M. Vasei, Y. Sang, H. Liu and J. P. Claverie, *ACS Appl. Mater. Interfaces*, 2016, **8**, 1903–1912.

59 S. Zhu, F. Yao, C. Yin, Y. Li, W. Peng, J. Ma and D. Zhang, *Microporous Mesoporous Mater.*, 2014, **190**, 10–16.
60 A. Annamalai, P. S. Shinde, A. Subramanian, J. Y. Kim, J. H. Kim, S. H. Choi, J. S. Lee and J. S. Jang, *J. Mater. Chem. A*, 2015, **3**, 5007–5013.
61 L. Jia, J. Xie, C. Guo and C. M. Li, *RSC Adv.*, 2015, **5**, 62611–62618.
62 K. C. Christoforidis, T. Montini, E. Bontempi, S. Zafeiratos, J. J. D. Jaén and P. Fornasiero, *Appl. Catal., B*, 2016, **187**, 171–180.
63 Y.-p. Li, F.-t. Li, X.-j. Wang, J. Zhao, J.-n. Wei, Y.-j. Hao and Y. Liu, *Int. J. Hydrogen Energy*, 2017, **42**, 28327–28336.